Methodological framework for determining vertical angular variances of terrestrial laser scanners

Jakob Hummelsberger[1], Omar AbdelGafar[1], Derek Lichti[2], Christoph Holst[1]

[1]Chair of Engineering Geodesy, TUM School of Engineering and Design, Technical University of Munich, Munich, Germany
{jakob.hummelsberger, o.abdelgafar, christoph.holst}@tum.de
[2]Department of Geomatics Engineering, Schulich School of Engineering, University of Calgary, Calgary, Canada
ddlichti@ucalgary.ca

Keywords: TLS, uncertainty, convolution, simulation, profile measurements, VCM.

Abstract

Information on the precision of TLS observables is limited. While the range measurement precision can be modeled with respect to the intensity measurement nowadays, the precision of the angular observations still relies on the claims of the manufacturer. This contribution proposes a method to determine the vertical angular variance of a TLS using profile measurements. Supported by a simulation, which serves as proof-of concept, the methodology is laid out. In the end, measurements with a *Z+F IMAGER® 5016A* are evaluated. A dependency of the angular standard deviation on the rotational speed of the beam deflection unit is observed. The estimation precision of the angular standard deviation is high with consistent values for differing ranges. The estimated angular standard deviations are much lower than the claims of the manufacturer starting with roughly 2” for the slowest rotating settings, up to 4” for the fastest. All this can be achieved by scanning a reflectivity target with at least two adjacent fields of different homogeneous reflectivity. This needs to be aligned to the scanner to reduce and eliminate as many contributing error sources as possible. The target itself provides the fields and the transitions needed to perform the in-situ estimation of the angular precision.

1. Introduction

Terrestrial Laser Scanners (TLS) play a prominent role in the field of engineering geodesy. The ability to capture the surroundings with millions of points per second while maintaining a high level of detail allows the usage of TLS in a broad variety of fields (Muralikrishnan, 2021; Sabzali and Pilgrim, 2025). Whether it is standard tasks like reality capture (Franceschi et al., 2009) and for example derived products like crop-height estimations (Hoffmeister et al., 2016) or point cloud based deformation analysis (Lindenbergh and Pietrzyk, 2015; Holst and Kuhlmann, 2016), TLS are already widely used. While some tasks have only minor requirements on the measurement precision of the instrument, others are in need of precise knowledge of the underlying precisions (Muralikrishnan, 2021).

Especially when estimating parameters and stating claims that are based on TLS observations, the correct input precision is a pre-requisite in order to be able to provide the correct significance and confidence measures for them. This is true for example for the point cloud based deformation analysis, where it must be clear whether a detected change is significant with respect to the measurement precision or not. A study by Jurek et al. (2017) shows the impact of the input stochastic model on the significance test. For comparable polar measurement systems like the Total Station (TS), the precision problem is solved by repeatedly measuring the same point and building empirical stochastic characteristics (ISO, 2018). This cannot be applied to TLS, as they are not capable of ensuring that the same point is measured multiple times (Holst and Kuhlmann, 2016).

The investigations into the accuracy of TLS began with first approaches to calibration parameters and accuracy determination by Lichti et al. (2000). With that, TLS can look back onto a history of accuracy related research of more than 25 years. Our investigations aim to fill the Variance-Covariance-Matrix (VCM) of TLS, which are a polar measurement system. The polar measurements consist of two angular observations, one horizontal φ and one vertical θ, measured by angular encoders, and the range r determined by a laser based distance measurement unit (Muralikrishnan, 2021). Latter one works based on pulse-based, phase-based or hybrid principles (Rüeger, 2012; Maar and Zogg, 2014). To fill the diagonal of the VCM, the variance of each observation has to be known. The off-diagonal is filled with the covariances. This contribution focuses on the estimation of the VCM entries regarding the variance of the vertical angle θ. Our study answers following research questions:

- How to derive a data processing method to estimate the vertical angular variance?
- What measurement setup is needed to estimate the vertical angular variance?
- How do vertical angular variances differ for different scanner settings with investigated TLS?

The paper is structured as follows: Section 2 explains the state of the art, followed by the methodology and simulation in Section 3. The results are summarized and discussed in Section 4 with a final conclusion in Section 5.

2. State of the art

For a long time, filling the diagonal of the VCM of observations relied on manufacturer’s claims provided in data sheets. This dependency stems from the fact that most TLS are a so called black-box system (Holst and Kuhlmann, 2014). Anyhow, measurements of a TLS are influenced by a multitude of errors. The domains these errors originate from are summarized by Soudarissanane et al. (2011) into four categories: instrument, atmosphere, object and observation geometry.

This contribution has been peer-reviewed. The double-blind peer-review was conducted on the basis of the full paper.
https://doi.org/10.5194/isprs-annals-XI-1-2026-363-2026

Instrumental errors comprise not only systematics, which can be reduced by calibration (García-San-Miguel and Lerma, 2013), but also random errors (Sabzali and Pilgrim, 2025). Latter are subject of this contribution. The corrections for the atmospheric propagation delay by Ciddor (1996) can be applied to TLS as well as for TS because of the similar ranging principle. The influences of the scanned object and its properties are examined by Boehler et al. (2003); Zámečníková et al. (2014) and the effect of the observation geometry by Zámečníková and Neuner (2018). Wujanz et al. (2017) developed a model that determines the noise of the range measurement based on the measured intensity, which is the product of all the previously mentioned error sources. This allows one third of the diagonal of the VCM to be filled. Range correlations are subject of ongoing research with the most prominent approach being the modeling of the overlap of neighboring laser footprints (Jurek et al., 2017; Schmitz et al., 2020).

The VCM entries regarding the angular precision, however, have not yet been investigated. While some approaches exist that use target center estimations (TCE) and the repeatability of them, Boehler et al. (2003) and Medić et al. (2019) claim that this results in the precision of the TCE. The TCE precision is based on all points on the target and investigated by Janßen et al. (2019); Medić et al. (2019). The diagonal in a VCM is filled with the precision of each individual observation. Hence, the TCE approach is unable to provide the VCM entries.

Summarizing, while much effort has been put into analyzing range uncertainty, partly including correlations, research regarding angular uncertainty of TLS only exists limitedly. This led to the development of a method to determine the angular precision of TLS with as least pre-processing as possible. This is required to not smooth over the noise of the individual observations. Our proposed method estimates the accumulation of all random effects influencing the angular observation.

3. Methodology

This section describes the methodology developed to determine the vertical angular variance σ_θ^2 of a TLS. Section 3.1 introduces a convolution analogy, which the methodology is based on. Section 3.2 briefly explains the choice of target used in this contribution. The workflow is explained in Section 3.4, based on an analysis of simulated observations from Section 3.3.

3.1 Methodological background

With our approach, we do not directly observe the vertical angular observation precision, quantified by the standard deviation σ_θ. Instead, we make use of the fact that σ_θ is also correlated to the measured intensity i. This dependence between the angular noise and the intensity can be explained using the analogy between the profile scanning of a TLS and a one dimensional convolution. In the discrete case, it holds (Tenoudji, 2016):

$$i(\theta) = h * x = \sum_{\zeta=-\infty}^{\infty} x(\zeta)h(\theta - \zeta). \tag{1}$$

Here, $i(\theta)$ equals the resulting intensity, h function 1 / the system, x function 2 / the scene and θ the vertical angle. At each shift of the system h, the two functions are integrated over by the summation index ζ. The laser footprint and its distribution are represented in Eq. (1) by h – the system impulse response.

Intensity observations could be simulated according to Eq. (1) if the exact scene x and laser beam size and distribution h are known. On the right side of Eq. (1), two error sources are relevant: First, the noise of the intensity measurement itself $\sigma_{i,meas}$. This noise source is always present and directly affects the intensity observation i. Second, an angular noise σ_θ. This noise in the shift of the laser beam h across the scene x influences the intensity i indirectly and with one condition: A change in intensity i caused by an angular error can only occur if scene x changes in the area that overlaps the laser beam footprint. If the scene stays homogeneous, an angular change does not yield an intensity change. The intensity noise component caused by the angular precision σ_θ is named $\sigma_{i,ang}$.

The law of variance propagation,

$$\sigma_{i,total}^2 = \sigma_{i,meas}^2 + \sigma_{i,ang}^2, \tag{2}$$

states, that if two variables are independent of each other, one can be derived as long as the other is known. Hence, the knowledge of the intensity measurement precision $\sigma_{i,meas}$ allows the reduction of the intensity measurement component $\sigma_{i,meas}^2$ from the total intensity variance $\sigma_{i,total}^2$. This leaves the intensity precision component $\sigma_{i,ang}$. This leftover intensity noise has its origin in a false angular measurement and can be converted back to σ_θ.

3.2 Target

Based on the preceding considerations, a scene x needs to be chosen which allows a controlled realization of the two intensity noise components. The target of choice is a four field intensity target, which is shown in Figure 1. It is a planar surface of four different calibrated reflectivities. The fields are made from *Zenith Lite*™ material (SphereOptics GmbH, 2024). Observed are vertical profiles of the target oriented as shown in Figure 1.

Figure 1. Target for the determination of the angular precision. Target size $\approx 100 \times 100$ cm.

The fields provide the two components necessary for the proposed method. On the one hand, there are the homogeneous fields wherein an angular error does not yield a intensity change. Here, the quantification of the intensity measurement noise $\sigma_{i,meas}$ is possible. On the other hand, they provide three sharp transitions. When the laser spot overlaps these and an angular error is made, the intensity i changes. Hence, the angular noise manifests itself as $\sigma_{i,ang}$. Because the intensity measurement noise $\sigma_{i,meas}$ is always present, the observed intensity noise in the transition is the accumulation of $\sigma_{i,ang}$ and $\sigma_{i,meas}$.

The consideration of only two measurement errors and influences on the final observation is a simplification. In the real world, numerous effects influence the observations. However, most of them can be reduced or eliminated by elaborate setups,

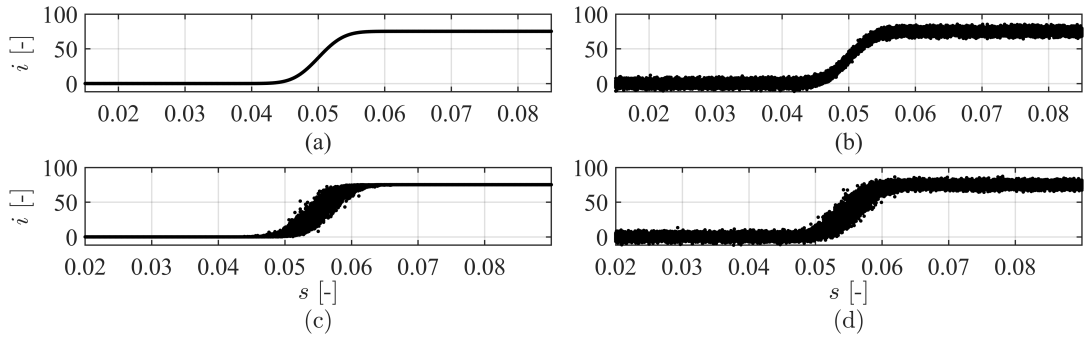

Figure 2. Simulated intensities by convolution. (a) Both noise components disabled. (b) Only intensity measurement noise $\sigma_{i,meas}$ enabled. (c) Only shift noise σ_s enabled. (d) Both noise components σ_s and $\sigma_{i,meas}$ applied.

as holds for the range and angle of incidence effects. By aligning the planar target to be perpendicular to the laser beam, both can be reduced. Due to the planarity, a full elimination of both effects can only be achieved for one single spot. The center transition is chosen to be the spot at which angle of incidence equals zero. The other transitions have neither zero incidence angle, nor do they have the same range as the center. For proof, our investigations on observed data showed no significant influence on the angular precision estimate. This is due to the in-situ nature of the proposed method and the choice of the intensity i.

The range effect on the intensity with $i \propto 1/r^2$ is negligible in this contribution due to the measurement geometry allowing only minor differences in r. The beam-size does not change between fields, because all observed surfaces are in one plane.

3.3 Simulated observations

Before we investigate real observations, we conduct a simulation. This simulation realizes the convolution analogy with the addition of two noise sources, following our explanations in Sections 3.1 and 3.2. The simulated intensities are further used in Section 3.4 to explain each step of the workflow in detail.

The simulation is modeled as linear system where the system's impulse response h represents the full accumulation of effects from the laser beam, optics, atmosphere etc. The beam is simulated as Gaussian curve and the target represented as step function. Because the simulation is done on a linear scale without specific unit, the angle θ is replaced by a neutral variable s. It represents the shift of the impulse response of the system. The precision of the angular observation is represented in the simulation by σ_s. The simulation of the observation data is done by an implementation of a convolution, which allows the introduction of two noise sources $\sigma_{i,meas}$ and σ_s.

The first noise source $\sigma_{i,meas}$ is added onto the result of the convolution afterwards. In the function, this noise component is created with a random number generator tuned to put out normally distributed values with the standard deviation specified as input. The second noise source σ_s is created with a random number generator producing normally distributed values, too. The second random variable is tuned to put out integer values that are added onto the shift parameter in the convolution process. Here, integers are necessary to shift the discrete signals by full increments. The noise source σ_s results in $\sigma_{i,ang}$.

The error free case is shown in Figure 2(a). It is the convolution of the laser footprint, represented as Gaussian bell, and a step function with its center at $s = 0.05$. This case depicts the simulated observations of a step function without intensity measurement noise $\sigma_{i,meas}$ and angular noise $\sigma_\theta = \sigma_s$. Enabling only the intensity measurement noise with an amplitude of $\sigma_{i,meas} = 3$ yields Figure 2(b). Over the whole simulation length, the same noise amplitude is visible in the intensity i. Figure 2(c) shows the effect of only enabling the shift noise σ_s, which represents the angular noise σ_θ. In the homogeneous regions, the shift-error has no influence on the intensity i. Once the laser spot begins to overlap the step function, the intensities get noisy. This is the manifestation of $\sigma_s = \sigma_\theta$ in $\sigma_{i,ang}$.

The combination of the noise sources in the simulation of the observations can be seen in Figure 2(d). Both characteristics are visible. The constant noise level in the homogeneous parts and the accumulation of both components in the transition. The combined case provides the simulated observations on which the workflow is laid out in detail.

3.4 Derived workflow

The workflow developed in this project uses vertical profiles of the intensity target (Figure 1) as input and is shown in Figure 3. In this section, the individual steps are explained in detail with figures depicting the analysis of the simulated observations from previous section. Because one profile would not provide enough observations for stochastic estimates, numerous profiles are combined to one data set of observations. In the simulation, 50 profiles are independently simulated and combined.

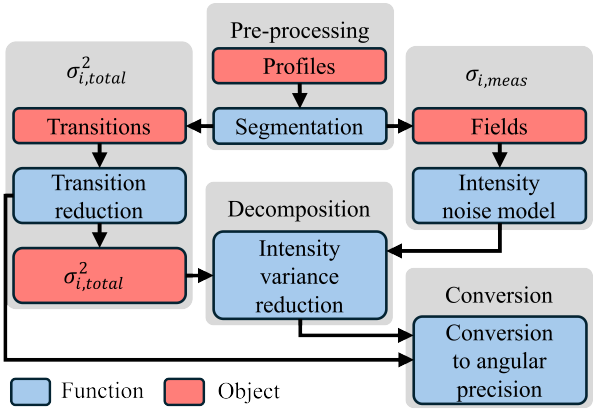

Figure 3. Workflow of proposed method to determine the angular precision of profile measurements.

Profiles & segmentation To independently quantify the intensity noise components, a separation of the data into fields and transitions is necessary. The fields are required to estimate $\sigma_{i,meas}$ and the transitions for $\sigma_{i,total}$. All observations are

sorted with respect to their vertical angle measurement θ and the differences Δi of intensity measurements are taken. The differences Δi of adjacent observations are the highest in the transition centers, allowing their approximation by a peak detection. The full transition is gathered by applying a margin in positive and negative angular direction. It is set to be a multiple of the claimed laser beam size at measured distance. A value of 5 times the beam size in both directions proved to be sufficient for profile scans.

In case of the simulation, The simulated observations consist of only one transition and the input intensity measurement noise $\sigma_{i,meas}$ is known. Hence, the segmentation is not necessary for the simulated observations.

Fields & intensity noise model For n transitions, $n+1$ fields are segmented. The fields are further processed into the intensity measurement noise model. This is done with the fields of homogeneous reflectivity, because here an angular error does not result in an intensity change. Contrary to the expected noise in the angular observations, all observations in profile mode are claimed to be done at the same vertical angular readings for every profile. The noise information is still accessible in the intensity noise, which is not binned like the angles. The standard deviation of the intensity and the mean intensity are calculated for each individual angular reading. This yields a mean intensity and a mean standard deviation of the intensity measurement for each field. Finally, a linear model is fitted through the results of all fields. The result is an intensity measurement noise model in dependence on the measured intensity.

Transitions The n transitions include the information on the total intensity variance $\sigma^2_{i,total}$, which is the accumulation of $\sigma^2_{i,meas}$ and $\sigma^2_{i,ang}$. Before the variance can be quantified, the transitional trend needs to be estimated and removed. The reduction function and its gradient is required in the conversion from intensity noise $\sigma_{i,ang}$ to angular noise σ_θ.

A purely mathematical approach is chosen. The 4-parameter-logistics (4pl) function (Rodbard, 1974)

$$f(x) = d + \frac{a-d}{1+(\frac{x}{c})^b}, \tag{3}$$

with a = lower convergence, b = steepness of transition, c = center of transition, d = upper convergence, $x = s$ (simulation) / θ (profile), is fitted using a trust-region based non-linear Least Squares adjustment (Coleman and Li, 1996). The 4pl function was chosen because it fulfills the requirements of a symmetrical logistics function with direct access to interpretable parameters. The symmetry requirement originates in the assumption that beam distribution and scene are symmetric, too.

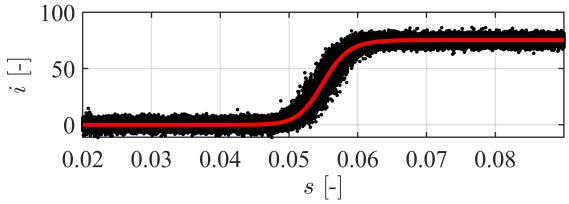

Figure 4. Simulated input data with both noise components enabled (black). 4pl fit of the input data (red).

Figure 4 depicts a 4pl fit of simulated intensity observations with both noise sources enabled. The observations are simulated with a Gaussian and a step function. The resulting error function has no closed form evaluation. Hence, the 4pl fit cannot fully correspond to the simulated data. This must be kept in mind for further evaluations, as it is one limitation of using the 4pl model.

Transition reduction Reducing the transitional trend reveals the total intensity noise amplitude in the transition. For both noise components enabled, the reduced intensities are as shown in Figure 5.

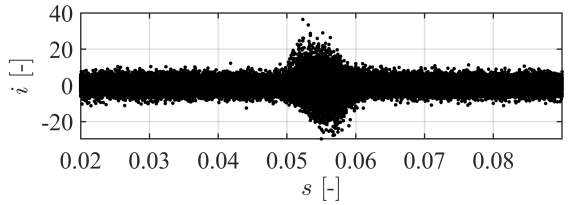

Figure 5. Simulated intensities reduced by the transitional trend from the fitted 4pl transition model.

The homogeneous parts only show the noise amplitude which is set by the intensity measurement noise component $\sigma_{i,meas}$. In the transitional area with its center at $s = 0.055$, the total noise increases because of the influence of the shift error σ_s.

Total intensity variance & intensity variance reduction Next, the variance of the reduced intensities is calculated. In both, simulation and profile measurement, this is a matter of finding all observations at each s in the simulation, or θ for profile scans, and calculating the variance of them. The resulting total intensity variances $\sigma^2_{i,total}$ are depicted in Figure 6.

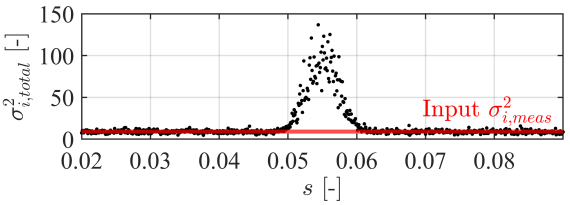

Figure 6. Variances $\sigma^2_{i,total}$ of reduced intensities (black). In addition, the input intensity measurement variance $\sigma^2_{i,meas}$ (red).

Figure 6 not only displays the total intensity variance $\sigma^2_{i,total}$ but additionally the input of the intensity measurement variance $\sigma^2_{i,meas}$ (red). From Eq. (2), the law of variance propagation, the next step is to reduce the total intensity noise by the component originating in the intensity measurement itself. In the case of the simulation, this is a constant value. For the profile scans, the intensity noise model is applied to determine the intensity measurement variance $\sigma^2_{i,meas}$ for each θ. This involves using the unreduced mean intensity of the corresponding θ as the input to the intensity noise model. Because the total intensity variances $\sigma^2_{i,total}$ are a random process and the reduction is only valid in a mean sense, negative variances may appear. This happens in the homogeneous regions where the variances are distributed around the mean intensity measurement variance.

The area where the reduced variances might be reduced to negative values is omitted in the final estimation of the angular variances. Hence, the absolutes of all reduced variances are calculated to be true to the definition of variance. This provides the first limitation of proposed method. If the combined intensity variance $\sigma^2_{i,total}$ in the transitional area is not significantly higher than the variance from the intensity measurement, it is

possible to reduce the combined variance below zero, even in the non-omitted part. This leads to a falsified estimation of the angular precision due to the absolute. The reduced, absolute variances for the simulated case are shown in Figure 7.

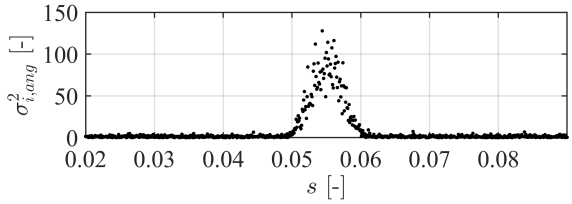

Figure 7. The absolutes of the total variances $\sigma^2_{i,total}$ reduced by the input intensity measurement variance $\sigma^2_{i,meas}$.

Figure 7 shows the intensity variance component which originated in the shift error σ_s. The left-over variances represented by intensities require conversion – in the simulation to the s domain to receive the shift error σ_s, in profile mode to the θ-domain to represent the angular error σ_θ.

Conversion to angular precision To convert the intensity variances to the angular domain, a function describing the change in shift or angle that would have resulted in the observed intensity change is needed. This function is found in the derivative of the reduction function (Figure 8), as it describes the gradient of the intensities with respect to the shift or angle.

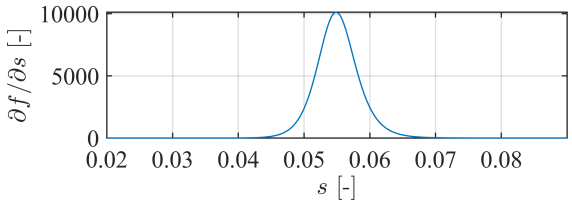

Figure 8. Derivative of the reduction function (4pl).

The intensity standard deviations $\sigma_{i,ang}$ – the square-root of the reduced variances $\sigma^2_{i,ang}$ – are divided by the derivative of the reduction function. For profile measurements, this can be written in units as:

$$\frac{[inc]}{\frac{[inc]}{[rad]}} = [inc] \cdot \frac{[rad]}{[inc]} = [rad]\,. \tag{4}$$

Therefore, by dividing the residual standard deviation of the reduced intensities $\sigma_{i,ang}$ by the derivative of the reduction function, the resulting error is in the angular domain for the profiles and the shift domain for the simulation.

Because the mathematical model does not completely fit the data at the edges of the transition, the derivative leads to wrong conversions there. Furthermore, the intensity variances at the edges of the transition are falsified because of taking their absolutes in the previous step. This is solved by specifying a sensitive area where the fit of the reduction function approximates the data well. A thresholding is applied defining the sensitive area as region where the derivative of the reduction function is greater than half the height of its maximum value. The data outside the sensitive area is omitted in the final estimation of the angular variances.

Figure 9 shows the resulting shift error σ_s (black) as well as the input shift error σ_s (red) and the mean σ_s (green) determined

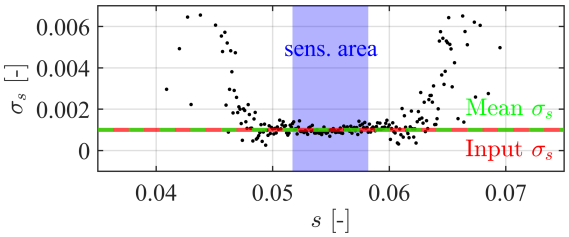

Figure 9. Converted intensity standard deviations to shift error σ_s (black). Simulation input (red) and output (green) shift noise level σ_s and sensitive area (blue).

from the data points in the sensitive area (blue). Numerically, the input shift error was set to $\sigma_{s,in} = 0.001000$. The output of this specific run equaled $\sigma_{s,out} = 0.001005$.

The simulation is a random process because both error sources are randomly generated. Therefore, fluctuations in the results are expected. A test of 5000 individual simulation runs provided a mean determined shift error of $\sigma_s = 0.001003$ with a standard deviation of 0.000016.

4. Results

This section presents the results of the profile measurements conducted in this project. Section 4.1 characterizes the TLS used as well as details about the setup. Section 4.2 presents all intermediate steps for one setting in detail and a comparison between settings at the end.

4.1 Experiment characteristics

The laser scanner, which is examined in this contribution, is the *Z+F IMAGER® 5016A* from Zoller + Fröhlich GmbH (2022). In the experiments, only a few of the available settings are investigated in the profile mode. These settings and their key parameter, the vertical rotational speed ω_θ, are summarized in Table 1. The angular precision claimed by the manufacturer is $\sigma_\theta \leq 14.4$” (Zoller + Fröhlich GmbH, 2022).

Resolution	Quality	ω_θ [rps]	Name
Ultrahigh	Speed+	54.67	UHQL
1.6 mm @ 10 m	Balanced	27.32	UHQN
	Quality+	13.65	UHQH
	Quality++	6.82	UHQP
Extr. high	Balanced	27.32	EHQN
0.6 mm @ 10 m	Quality+	13.65	EHQH
	Quality++	6.82	EHQP

Table 1. Investigated scan settings for the *Z+F IMAGER® 5016A* in profiler mode. Resolution and the vertical rotational speed ω_θ in rotations per second [rps] as indicated by scanner.

The center transition between black and white is aligned to the height of the trunnion axis using a Leica TS60 (Leica Geosystems AG, 2020). The TS60 is also used to level the transitions and align the target perpendicular to the scanner to minimize angle of incidence effects that could perturb the measurements.

A study by Janßen et al. (2021) investigated the effects in the warm-up phase of a similar TLS. To reduce any of the thermal effects, a panoramic scan with a resolution of 0.6 mm @ 10 m and quality setting *Quality+* is conducted to warm up all components. Subsequently, at least 3000 profiles with each of the settings listed in Table 1 are scanned with the scanner locked in the horizontal rotation. This is done at approximately 10 m and 17 m. Only 1000 profiles are used for further analysis.

4.2 Angular variance results

The intermediate steps and results are exemplarily displayed for setting EHQP (see Table 1) and a range of 10 m.

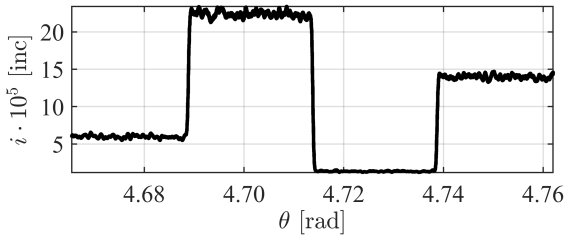

Figure 10. 1000 raw profile measurements of the target shown in Figure 1 with setting EHQP (see Table 1).

Figure 10 depicts the raw data of setting EHQP at 10 m, as intensity i against vertical angle θ. Directly visible are the systematic fluctuations in the fields which are supposed to be homogeneous. Due to this, the standard deviation and mean intensity for the intensity measurement noise model must be calculated per angle, rather than from all measurements per field.

Segmentation The sorted intensity differences Δi used in the segmentation step are shown in Figure 11 (black). The detected peaks are plotted in blue and in red the cutting lines, determined from the peaks and the margin based on the claimed beam size.

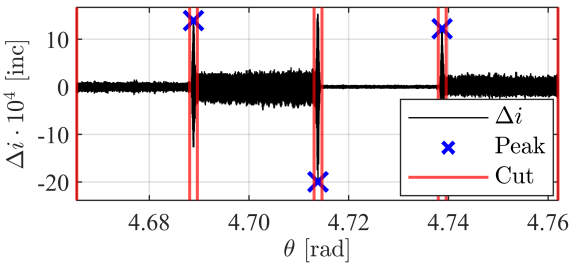

Figure 11. Segmentation process. Intensity differences Δi sorted by vertical angle θ in black. Detected peaks in blue and the cutting lines by adding margin to peaks in red.

Fields & intensity noise model The segmented fields are processed into the intensity measurement noise model. In the case of real measurements, this is not constant but rather a function of the measured intensity. The relation between the mean intensity i and the mean intensity standard deviation $\sigma_{i,meas}$ based on the fields of the target is shown in Figure 12.

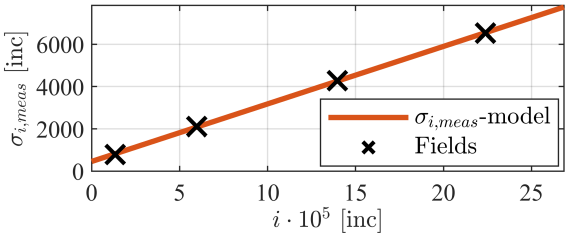

Figure 12. In-situ intensity measurement noise model for setting EHQP at 10 m from four fields of homogeneous reflectivity.

Each black data point in Figure 12 represents one mean intensity i per field and its corresponding mean intensity standard deviation $\sigma_{i,meas}$. The functional model chosen for the intensity measurement noise model is a linear one. A first-degree polynomial is fitted using a Least-Squares estimation. The model parameters change for each setting and distance, but the linear relation held true for all observed combinations. The intensity measurement noise model of setting EHQP at 10 m is represented by $\sigma_{i,meas}\,[\text{inc}] = 0.002721 \cdot i\,[\text{inc}] + 458.5\,[\text{inc}]$.

Transitions Processing of the transitions starts with the estimation of the transitional trend by fitting the 4pl functional model of Eq. (3) into the segmented transitions. The initial parameters for the 4pl model are derived from the observations. The upper and lower convergences a and d, as well as the center c, are directly determined from the observations. The steepness parameter b is calculated from the length of the transition and the difference $d - a$. The transitions and their fitted transitional trends are plotted in Figure 13. The 4pl fits (red) approximate the data (black) well in this setting. A small fraction of the other settings struggles to provide a good fit of the mathematical model. The results of fits that do not work are left out in the final results. Figure 13 shows the increase in intensity noise due to the angular noise in the transition as widening of the raw intensity observations. In the following, each of the three transitions is depicted in its own subplot.

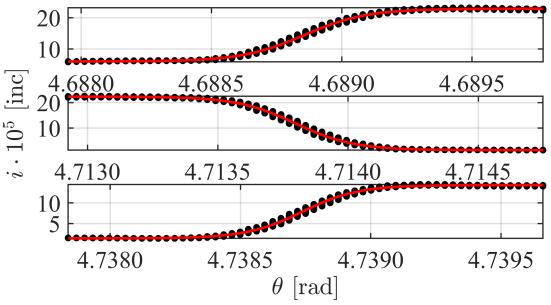

Figure 13. Raw observations of the segmented transitions (black) with their 4pl fits (red). Corresponds to Figure 4.

Transition reduction Reducing the transitional trend leaves the residuals plotted in Figure 14. The color of each reduced intensity is chosen according to the profile number it originates from. This allows the analysis for drifts or systematics.

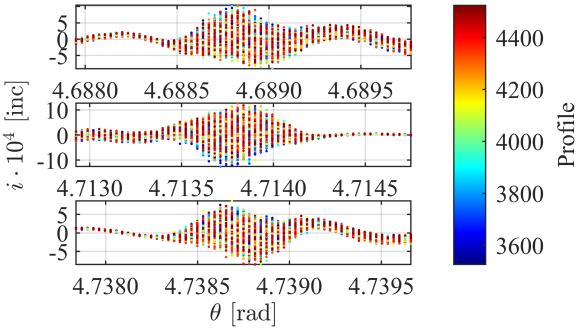

Figure 14. Reduced intensities of the segmented transitions. Coloring according to profile number. Corresponds to Figure 5.

The coloring of the residuals shows that no systematics or drifts are present. The bulge in the transition is the result of the combination of intensity measurement noise $\sigma_{i,meas}$ with angular noise σ_θ, which results in intensity noise $\sigma_{i,ang}$. On the sides of the transitions, only the intensity measurement noise is present. There, one can see the different noise levels of different intensities. The left over fluctuations in the residuals are a result of the limitations of the fitted 4pl transition model.

This contribution has been peer-reviewed. The double-blind peer-review was conducted on the basis of the full paper.
https://doi.org/10.5194/isprs-annals-XI-1-2026-363-2026 | © Author(s) 2026. CC BY 4.0 License.

Total intensity variance & intensity variance reduction After the reduction of the transitional trend, the total intensity variance $\sigma^2_{i,total}$ of the reduced intensities is calculated. The total intensity variance is reduced by the intensity measurement variance $\sigma^2_{i,meas}$ from the previously determined intensity measurement noise model. Due to the scale of the figures, the difference between total intensity variances $\sigma^2_{i,total}$ and the intensity variances reduced by the intensity measurement noise model $\sigma^2_{i,meas}$ is not visible. Therefore, only the reduced intensity variances $\sigma^2_{i,ang}$ are shown in Figure 15. These now represent the intensity variances $\sigma^2_{i,ang}$ which are a result of the angular noise σ_θ.

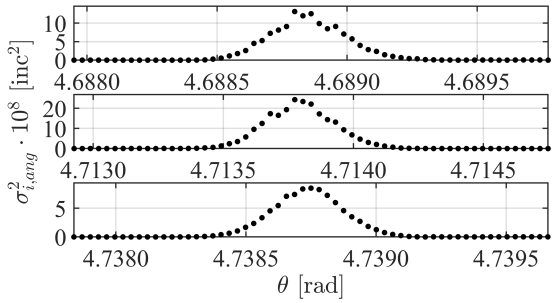

Figure 15. Intensity variances $\sigma^2_{i,total}$ reduced by the intensity measurement variance $\sigma^2_{i,meas}$ determined by intensity measurement noise model (Figure 12). Corresponds to Figure 7.

Conversion to angular precision The square-root of these reduced variances are taken. The resulting intensity standard deviations $\sigma_{i,ang}$, which are solely caused by erroneous angular measurements, are further divided by the derivative of the fitted 4pl model. The result is the converted standard deviation σ_θ – now in the angular domain. The resulting angular standard deviations of each transition are depicted in Figure 16.

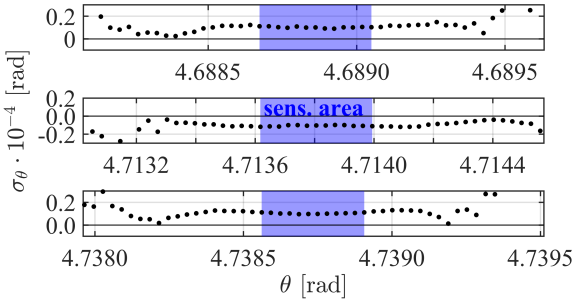

Figure 16. Resulting intensity standard deviations converted to angular standard deviation σ_θ (black). Sensitive area (blue) from thresholding the derivative. Corresponds to Figure 9.

The blue area is the sensitive area. The second transition results in negative values because the derivative is negative. For the mean standard deviation of the setting, the absolutes of all three transitions are used. The mean angular errors per transition are numerically $\sigma_\theta = 2.11” = 0.01021$ mrad for the transition between dark-gray and white, $\sigma_\theta = 2.13” = 0.01032$ mrad from white to black and $\sigma_\theta = 2.12” = 0.01026$ mrad for the transition between black and light-gray.

With all settings and distances estimated as described in Section 3, the dependency of the mean angular standard deviation on the rotational speed of the scanner is drawn. Figure 17 shows all setting-distance combinations. Each data point represents the mean angular standard deviation of the vertical angle measurement of three transitions with exception of two. These two are a result of settings where only two of the three transitions are usable, because the 4pl fit did not work. In addition to the mean angular standard deviation, the standard deviation of each data point calculated from the results of the individual transitions is added in black scaled with a factor of 2.

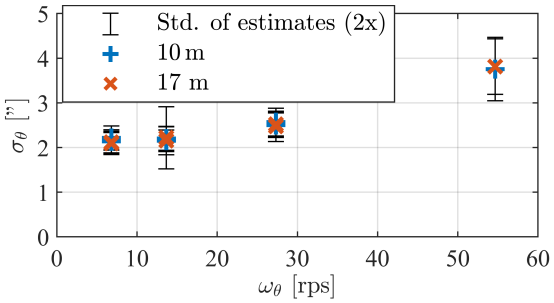

Figure 17. σ_θ in dependence of the vertical rotational speed of the beam deflection unit. Colored according to measurement range. Standard deviations of estimates, scaled 2 times, in black.

We color-coded the data points in Figure 17 according to the distance they were measured at. As expected, there are no significant differences detectable since the angular variance should stay unaffected from the measured range.

5. Conclusion

We propose a straight-forward methodology to determine the vertical angular variance, i.e., its precision, of TLS. The precision of the estimation as well as the consistency is very high. No pre-processing like georeferencing or transformations are necessary. It is purely based on raw data directly taken from the scanner, segmented and then analyzed.

The setup requirements are minimal. Only two adjacent fields of homogeneous reflectivity with a sharp transition in between are needed as long as the scanner intensity measurement noise model is linear. A stable ground support is advised as any changes in the scanners orientation are directly translated into the result.

Generally, the achieved results meet the expectations, like the dependency of precision on the rotational speed, and the independency on the measured range. Anyhow, the estimated angular precisions of $\approx 2”$ to $\approx 4”$ are much lower than the manufacturer claims. Since our method relies on the pre-elimination of non-considered error sources (e.g., range and angle of incidence, etc.), the angular precision could be even higher than in the case of this contribution.

In this contribution, the two noise sources are assumed to be independent, disregarding any possible correlation. Further investigations should be aimed towards estimating the maximum impact of possible correlations.

The fitting of the 4pl transition model works in most cases. Because it is purely mathematical, there is no physical knowledge of the trueness. Simulating the transition using a step function and knowledge of the beam distribution would provide a physically backed reference transition that consistently works. This requires better knowledge of the beam size and distribution.

This contribution has been peer-reviewed. The double-blind peer-review was conducted on the basis of the full paper.
https://doi.org/10.5194/isprs-annals-XI-1-2026-363-2026 | © Author(s) 2026. CC BY 4.0 License.

Acknowledgments

This research was funded by the German Research Foundation (DFG) under grant number 490989047, DFG FOR 5455 ”TLS-Defo”.

References

Boehler, W., Vicent, M. B., Marbs, A. et al., 2003. Investigating laser scanner accuracy. *Proceedings CIPA XIXth International Symposium*, 34, 696–701.

Ciddor, P. E., 1996. Refractive index of air: new equations for the visible and near infrared. *Appl. Opt.*, 35(9), 1566–1573. doi:10.1364/AO.35.001566.

Coleman, T. F., Li, Y., 1996. An Interior Trust Region Approach for Nonlinear Minimization Subject to Bounds. *SIAM Journal on Optimization*, 6(2), 418–445. doi:10.1137/0806023.

Franceschi, M., Teza, G., Preto, N., Pesci, A., Galgaro, A., Girardi, S., 2009. Discrimination between marls and limestones using intensity data from terrestrial laser scanner. *ISPRS J. of Photogramm. and Remote Sens.*, 64(6), 522-528. doi:10.1016/j.isprsjprs.2009.03.003.

García-San-Miguel, D., Lerma, J., 2013. Geometric calibration of a terrestrial laser scanner with local additional parameters: An automatic strategy. *ISPRS Journal of Photogrammetry and Remote Sensing*, 79, 122-136. doi:10.1016/j.isprsjprs.2013.02.007.

Hoffmeister, D., Waldhoff, G., Korres, W., Curdt, C., Bareth, G., 2016. Crop height variability detection in a single field by multi-temporal terrestrial laser scanning. *Precision Agriculture*, 17, 296–312. doi:10.1007/s11119-015-9420-y.

Holst, C., Kuhlmann, H., 2014. Aiming at self-calibration of terrestrial laser scanners using only one single object and one single scan. *J. of Appl. Geodesy*, 8(4), 295–310. doi:10.1515/jag-2014-0017.

Holst, C., Kuhlmann, H., 2016. Challenges and Present Fields of Action at Laser Scanner Based Deformation Analyses. *J. of Appl. Geodesy*, 10(1), 17–25. doi:10.1515/jag-2015-0025.

ISO, 2018. ISO 17123-5 Optics and optical instruments - Field procedures for testing geodetic and surveying instruments - Part 5: Total stations. Int. Organ. for Stand., Geneva, Switzerland.

Janßen, J., Kuhlmann, H., Holst, C., 2021. Assessing the temporal stability of terrestrial laser scanners during long-term measurements. *Contributions to Int. Conf. on Eng. Surveying*, 69–84. doi:10.1007/978-3-030-51953-7_6.

Janßen, J., Medic, T., Kuhlmann, H., Holst, C., 2019. Decreasing the Uncertainty of the Target Center Estimation at Terrestrial Laser Scanning by Choosing the Best Algorithm and by Improving the Target Design. *Remote Sens.*, 11(7), 845. doi:10.3390/rs11070845.

Jurek, T., Kuhlmann, H., Holst, C., 2017. Impact of spatial correlations on the surface estimation based on terrestrial laser scanning. *J. of Appl. Geodesy*, 11(3), 143–155. doi:10.1515/jag-2017-0006.

Leica Geosystems AG, 2020. Leica Nova TS60 – World’s Most Accurate Total Station. Available at: https://leica-geosystems.com/products/total-stations/robotic-total-stations/leica-nova-ts60 (Accessed: 25 Oct 2025).

Lichti, D., Stewart, M., Tsakiri, M., Snow, A., 2000. Calibration and testing of a terrestrial laser scanner. *Int. Arch. of Photogramm. and Remote Sens.*, 33(B5/2; PART 5), 485–492.

Lindenbergh, R., Pietrzyk, P., 2015. Change detection and deformation analysis using static and mobile laser scanning. *Appl. Geomatics*, 7(2), 65–74. doi:10.1007/s12518-014-0151-y.

Maar, H., Zogg, H.-M., 2014. Wfd–wave form digitizer technology, white paper. Available at: https://leica-geosystems.com/about-us/content-features/wave-form-digitizer-technology-white-paper (Accessed: 23 Oct 2025). Leica Geosystems AG, Heerbrugg, Switzerland.

Medić, T., Holst, C., Janßen, J., Kuhlmann, H., 2019. Empirical stochastic model of detected target centroids: Influence on registration and calibration of terrestrial laser scanners. *J. of Appl. Geodesy*, 13(3), 179–197. doi:10.1515/jag-2018-0032.

Muralikrishnan, B., 2021. Performance Evaluation of Terrestrial Laser Scanners – A Review. *Meas. Science and Technol.*, 32(7), 072001. doi:10.1088/1361-6501/abdae3.

Rodbard, D., 1974. Statistical Quality Control and Routine Data Processing for Radioimmunoassays and Immunoradiometric Assays. *Clinical Chemistry*, 20(10), 1255-1270. doi:10.1093/clinchem/20.10.1255.

Rüeger, J. M., 2012. *Electronic Distance Measurement: An Introduction*. Springer, Berlin. doi:10.1007/978-3-642-80233-1.

Sabzali, M., Pilgrim, L., 2025. A Comprehensive Review of Mathematical Error Characterization and Mitigation Strategies in Terrestrial Laser Scanning. *Remote Sens.*, 17(14), 2528. doi:10.3390/rs17142528.

Schmitz, B., Kuhlmann, H., Holst, C., 2020. Investigating the resolution capability of terrestrial laser scanners and its impact on the effective number of measurement. *ISPRS J. of Photogramm. and Remote Sens.*, 159(14), 41–52. doi:10.1016/j.isprsjprs.2019.11.002.

Soudarissanane, S., Lindenbergh, R., Menenti, M., Teunissen, P., 2011. Scanning geometry: Influencing factor on the quality of terrestrial laser scanning points. *ISPRS J. of Photogramm. and Remote Sens.*, 66(4), 389–399. doi:10.1016/j.isprsjprs.2011.01.005.

SphereOptics GmbH, 2024. Zenith Lite™ Reflexionstargets. Available at: https://sphereoptics.de/product/zenith-lite-targets/ (Accessed: 25 Oct 2025).

Tenoudji, F. C., 2016. *Analog and Digital Signal Analysis, From Basics to Applications*. Springer, Cham. doi:10.1007/978-3-319-42382-1.

Wujanz, D., Burger, M., Mettenleiter, M., Neitzel, F., 2017. An intensity-based stochastic model for terrestrial laser scanners. *ISPRS J. of Photogramm. and Remote Sens.*, 125(1), 146-155. doi:10.1016/j.isprsjprs.2016.12.006.

Zámečníková, M., Neuner, H., 2018. Methods for quantification of systematic distance deviations under incidence angle with scanning total stations. *ISPRS J. of Photogramm. and Remote Sens.*, 144, 268-284. doi:10.1016/j.isprsjprs.2018.07.008.

Zámečníková, M., Wieser, A., Woschitz, H., Ressl, C., 2014. Influence of surface reflectivity on reflectorless electronic distance measurement and terrestrial laser scanning. *J. of Appl. Geodesy*, 8(4), 311–325. doi:10.1515/jag-2014-0016.

Zoller + Fröhlich GmbH, 2022. Z+F IMAGER® 5016 User Manual V2.8. Zoller + Fröhlich GmbH, Simoniusstrasse 22, 88239 Wangen im Allgäu, Germany.